Precision defect integrated graphene as reliable support membrane for high-resolution cryo-transmission electron microscopy

Kshipra Sharma, Uriel López-Sánchez, Hugues Nury, Guy Schoehn, Claudine Darnault, Cécile Breyton, Camille Petit-Etienne, Céline Vergnaud, Wai Li Ling, Gilles Cunge, et al.

Carbon 230 (2024) 119625

Contents lists available at ScienceDirect

Carbon

journal homepage: www.elsevier.com/locate/carbon

Precision defect integrated graphene as reliable support membrane for high-resolution cryo-transmission electron microscopy

Kshipra Sharma [a], Uriel López-Sánchez [b], Hugues Nury [b], Guy Schoehn [b], Claudine Darnault [b], Cécile Breyton [b], Camille Petit-Etienne [c], Céline Vergnaud [d], Wai Li Ling [b,*], Gilles Cunge [c,**], Hanako Okuno [a,***]

[a] Univ. Grenoble Alpes, CEA, IRIG-MEM, 38000, Grenoble, France
[b] Univ. Grenoble Alpes, CEA, CNRS, IBS, Grenoble, France
[c] Univ. Grenoble Alpes, CNRS, CEA/LETI-Minatec, Grenoble INP, Institute of Engineering and Management University Grenoble Alpes, LTM, Grenoble, F-38054, France
[d] Univ. Grenoble Alpes, CEA, CNRS, Grenoble INP, IRIG-Spintec, 38000, Grenoble, France

ARTICLE INFO

Keywords:
Graphene
Wetting properties
Atomic defects
Hydrophilicity
Cryo-EM
Single particle analysis

ABSTRACT

Graphene is an excellent support film for high-resolution transmission electron microscopy (TEM) but its use with biological samples, notably in cryo-TEM, is hindered by its inherent hydrophobicity. Whereas surface treatments have been proposed to render graphene hydrophilic, they are often difficult to reproduce due to a lack of information on the structural changes that modify the wetting properties of graphene. This study aims to correlate the atomic structure of graphene with its wetting properties to allow a reproducible protocol to advance its application in cryo-TEM. We follow the change in the atomic structure of graphene as a function of low-energy hydrogen plasma treatment duration on monolayer graphene transferred onto TEM grids. With finely controlled plasma exposure, partial hydrogenation, monoatomic vacancies, and pores of a few nanometers are realized in the graphene. The introduction of defects (vacancies and pores) enables the formation of continuous layers of vitreous ice on TEM grids. Grids with defect-integrated graphene are reproduced and used in the vitrification of the mouse serotonin 5-HT_3 receptor, a membrane protein. Single particle analysis of the membrane protein on graphene compared to conventional holey carbon film give insight into the strengths and discretions in using graphene membrane for protein structural studies.

1. Introduction

Graphene has diverse applications, e.g. bioengineering and opto-electronics, due to its exceptional physical, chemical, mechanical, and surface properties [1–5]. In particular, graphene is an ideal support film for high-resolution transmission electron microscopy (HRTEM) due to its high electron transparency, good mechanical strength and high thermal and electrical conductivity, which enhance sample stability while mitigating radiation damage by the electron beam [6]. Use of graphene support film has yielded superior images of nanomaterials, including perovskite, quantum dots and carbon nanotubes [7,8].

On the other hand, the use of graphene support film in cryo-TEM for structural biology is far from common. Cryo-TEM is an important technique for solving native protein structures, essential for understanding protein function and for facilitating drug development. To be compatible with the vacuum in the electron microscope column, protein in solution is vitrified and imaged at near liquid nitrogen temperature in the frozen solid state. Cryo-TEM imaging yields 2D projections of the protein molecule in its native hydrated state. With a homogeneous sample, the projections can then be sorted into different orientations of the molecule with single particle anlaysis. A 3D reconstruction of the protein molecule can be obtained if the orientation space is sufficiently sampled and if the signal-to-noise ratio of the images allow accurate alignment of the particles. Inevitably, sample motion due to charging or buckling of ice upon electron irradiation, radiation damage, or protein denaturing at the air-water interface can compromise the resolution that can be achieved [9]. With its exceptional physical properties, use of graphene support film can potentially alleviate these

* Corresponding author.
** Corresponding author.
*** Corresponding author.
E-mail addresses: wai-li.ling@ibs.fr (W.L. Ling), gilles.cunge@cea.fr (G. Cunge), hanako.okuno@cea.fr (H. Okuno).

https://doi.org/10.1016/j.carbon.2024.119625
Received 14 May 2024; Received in revised form 18 July 2024; Accepted 10 September 2024
Available online 10 September 2024

problems and improve the resolution in cryo-TEM.

Indeed, use of graphene support membrane has proved very promising in cryo-TEM [10–15]. It has been shown that particle density as well as particle distribution can be significantly improved using a graphene support film [12], [15]. Sample movement is also considerably reduced. Moreover, radiation damage is migitated, allowing a longer exposure time for higher signal-to-noise ratio [16]. The use of a graphene support can also better control ice thickness to minimize background scattering from the ice layer [16]. Moreover, there is evidence that graphene helps to avoid protein denaturing at the air-water interface [17]. All these factors enhance the resolution achieved in cryo-TEM experiments.

Despite these benefits, the use of graphene in cryo-TEM remains limited. One of the main challenges is the hydrophobic nature of graphene, which originates from its sp^2 hybridized non-polar electronic structure, which has a low surface energy [18–20]. To circumvent this problem, hydrophilic graphene oxide flakes have been used [21]. However, the coverage of the grid by the flakes is not satisfactory. On the contrary, transferred graphene sheets can reliably cover most, if not all, of the TEM grid surface. To turn graphene hydrophilic, various surface treatments, such as UV/ozone treatment [16], chemical functionalization (with and without plasma) [11,13, 22], and hydrogen plasma treatment [15], or air glow discharge [23], have been employed. Nonetheless, the key parameters for tuning the wetting properties of graphene remains elusive, which hinders the routine adoption of graphene as a support membrane for biological samples.

This study aims to elucidate the structural changes that govern the change in wetting properties of graphene. Graphene monolayers were transferred onto TEM grids and plasma treatment was applied in a finely controlled fashion to introduce defects in the graphene. While inherent lattice defects and distortions from growth and processing may compromise device performance, deliberate and controlled integration of defects, e.g. pores, have enabled novel applications of graphene in filtration membranes, such as DNA sequencing, water desalination, and gas filtration [24–29]. In this work, we used low-energy hydrogen plasma because it allows controlled and selective etching of graphene structure [30–32] without causing direct sputtering damage to graphene when exposure is limited [33–35]. Actually, ultraviolet-ozone and oxygen plasma treatment have been found to induce contaminations and topological defects on graphene, respectively [36]. On the other hand, hydrogen plasma treatment has yielded hydrophilic graphene support suitable for cryo-TEM even though the underlying structural changes that accompany the change in the graphene wetting property have not been determined [15]. Here, we follow the effect of the hydrogen plasma on the atomic structure of graphene using aberration-corrected, monochromated HRTEM and Raman spectroscopy. Distinct atomic structures were attained with increasing plasma exposure.

The modified graphene grids were then used for cryo-TEM experiments on biological specimens. Bacteriophage T5 was used as a test sample to search for the best conditions that achieved a thin, uniform vitrified ice layer. Graphene grids with the atomic structure that yielded the optimal wetting property were then used for the vitrification of a membrane protein, the serotonin 5-HT_3 receptor. Results from single particle analysis of vitrified samples using treated graphene grids were compared with those frozen on conventional holey carbon grids.

2. Methodology/experimental

2.1. Sample preparation

2.1.1. Preparation of structure-modified graphene grids

A graphene monolayer grown by chemical vapor deposition (CVD) on a Cu foil substrate was purchased from Graphenea. The graphene surface was covered with a thin protective layer of poly-methyl methacrylate (PMMA). To transfer PMMA/graphene from the Cu substrate onto holey carbon TEM grids, we employed the metal dissolution method [8,37]. The substrate was etched away chemically in an aqueous solution of 0.2 M ammonium persulphate for 5 h. Subsequently, the floating PMMA/graphene layer was transferred to deionized water for thorough rinsing before being retrieved onto a TEM grid. The prepared PMMA/graphene grids were then dried and immersed in acetone and isopropanol to dissolve the PMMA layer.

All graphene grids were annealed under an oxygen environment at 150 °C for a few hours to eliminate the remaining hydrocarbon contamination on the surface. Whereas high temperatures (i.e., >300 °C) or prolonged annealing of graphene in an oxidative environment can lead to oxidation and defect integration in graphene [38], oxidative annealing of graphene at low temperatures can efficiently remove hydrocarbon contaminants by oxidation and breaking of the sp^3 C–H bond [39]. Therefore, in this work, we used oxidative annealing at 150 °C for 2–3 h for all graphene samples after the PMMA removal procedure. This temperature is low enough to avoid significant oxidation or defect generation while effectively minimize hydrocarbon contaminants, which allow the analysis of graphene at the atomic scale (HRTEM images and Raman spectra before and after annealing are found in Suppl. Fig. S1).

We used a Gatan plasma cleaner (Solarus Model 950) with a low-energy hydrogen plasma to modify the atomic structure of the graphene grids. The vacuum chamber was filled with 200 sccm of H_2 to maintain an operating pressure of 225 mTorr. The plasma was generated with a low radio frequency power of 65 W. To investigate the impact of the duration of hydrogen plasma treatment on the atomic structure of graphene grids, each grid was exposed individually to hydrogen plasma for varying durations. The modification in the atomic structure of graphene is then characterized by HRTEM.

2.1.2. Vitrification of biological specimens on graphene grids for cryo-TEM

We prepared vitrified samples of bacteriophage T5 and detergent-reconstituted mouse serotonin receptor (m5-HT_3) on the plasma-modified graphene grids. The T5 sample was prepared as described previously [40]. The sample contained 10^{13} phages/ml in 50 mM Tris (pH 7.5, 100 mM NaCl, 1 mM $MgCl_2$, and 1 mM $CaCl_2$). The m5-HT_3 sample was prepared as described by Grychowska et al. [41]. The membrane protein at 1 mg/ml was solubilized in 50 mM Tris pH 7.4, 125 mM NaCl and 0.02 % C12E9. Around 3 μL of the sample solution was applied to the plasma-modified graphene grids and plunged frozen in liquid ethane using a Thermo Fisher Vitrobot Mark-IV. Blotting time ranging from 3 s to 8 s was tested.

2.2. Characterization of plasma-modified graphene grids

Crystallinity of the graphene transferred onto TEM grids before and after plasma-induced structural modification was investigated using Raman spectroscopy. Raman spectroscopy is an efficient technique for characterizing structural irregularities such as the nature and density of defects in carbon-based materials on arbitrary substrates.

Raman spectra of the graphene monolayer across the holes on the TEM grids were recorded using an inVia Raman microscope from Renishaw with a power consumption of 150 W. The excitation laser had a wavelength of 532 nm and a spot size of 800 nm. Several spectra were recorded from various sites of the suspended graphene, each with an acquisition time of 20 s and signal accumulation over 4 cycles.

The atomic structure of the graphene grids was investigated by HRTEM before they were used as a support film for cryo-TEM sample preparation. We employed an aberration-corrected monochromated TEM (Titan Ultimate) with an 80 keV acceleration voltage to minimize knock-on damage to the graphene by the electron beam. Image sequences were captured using a Gatan Oneview CMOS detector. Twenty consecutive frames of 0.15 s were recorded and aligned for motion correction to enhance the signal-to-noise ratio in the final image.

To assess the wetting properties of the structure-modified graphene grids, we conducted water contact angle (WCA) measurements using a

GBX-digidrop instrument. Following the application of a 0.7 μl droplet of deionized water onto the graphene grid, an optical image was promptly captured using a camera integrated in the instrument. Four grids with pristine graphene were tested and 2 grids each for hydrogenated graphene and nanopore-integrated graphene grids. The deviation among different grids was found to be within ±5°, indicating good reproducibility of the results.

2.3. Cryo-transmission electron microscopy

Cryo-TEM imaging was conducted on a Thermo Fisher Glacios microscope operating at 200 keV. Movies of 40 frames were recorded on a Gatan K2 direct electron detector with a cumulated dose of ~40 e^-/A^2. The defocus value ranged from −0.7 μm to −2.3 μm. Particle picking was done with crYOLO [42] and data analysis was carried out with CryoSparc [43]. In each data set, several rounds of 2D classification, *ab initio* model reconstruction with three 3D classes, and heterogeneous refinement were performed. Visualisation of the model was done using Chimera [44].

3. Results and discussion

After the graphene monolayer was transferred onto the TEM grids, the grids were treated to remove the PMMA protective layer on the graphene and the remaining surface contamination. Each graphene sample was then exposed to hydrogen plasma for a controlled duration varied between 120 s and 132 s. While oxygen plasma can rapidly attack the atomic structure of graphene, hydrogen plasma reacts with graphene in progressive stages and allow controlled defect formation in the graphene. The atomic structure of graphene after the various exposure time was examined by aberration-corrected monochromated HRTEM imaging.

Fig. 1 shows HRTEM images of the graphene grids before and after hydrogen plasma treatment. Fig. 1a is a representative image of the graphene surface before hydrogen plasma treatment. The hexagonal close packed carbon atoms are clearly resolved. However, the surface is still partially covered by PMMA residuals (coverage is around 40 %), indicating that low-temperature annealing is insufficient to completely eliminate the PMMA coating.

Fig. 1b shows the graphene grid after exposure to hydrogen plasma for 2 min. The plasma treatment eliminated most of the PMMA while the graphene atomic structure was preserved. The treatment yielded a cleaner surface, where pristine area of around 30 nm^2 free of contamination can be routinely found.

Extending plasma exposure by 10 s (Fig. 1c) initiated the formation of carbon vacancies. Most vacancies corresponded to the removal of a

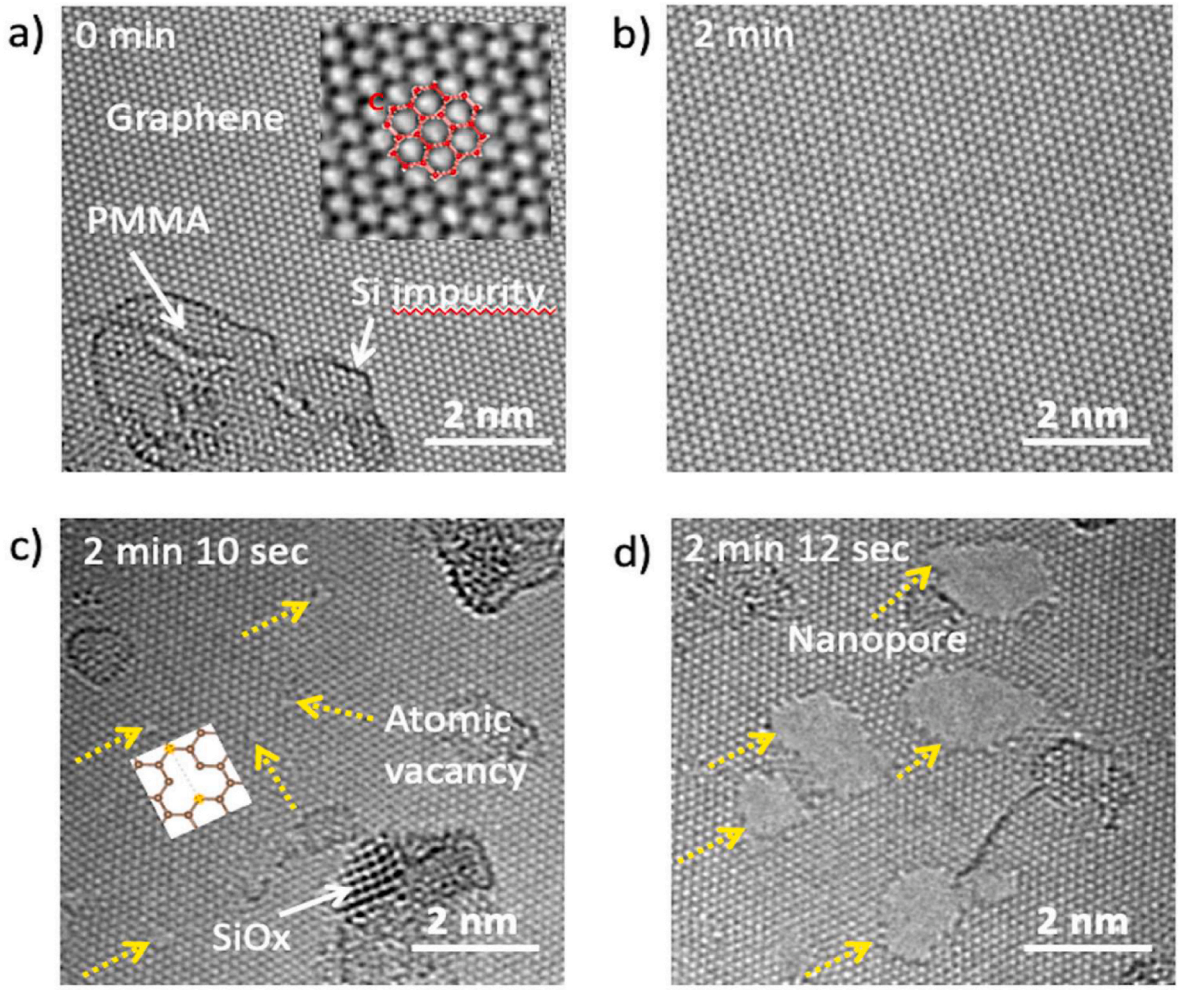

Fig. 1. High-resolution TEM images of graphene samples before and after hydrogen plasma exposure. (a) Graphene before plasma treatment displays a regular hexagonal close packed structure. Inset shows carbon atoms arranged in a hexagonal ring. (b) Graphene after 2 min of plasma exposure is mostly free of PMMA. While stacking faults are present, no point defects are observed. (c) Graphene after 2 min 10 s of plasma exposure. Vacancies are formed. They are primarily monoatomic, as shown in the inset. (d) Graphene after 2 min 12 s of plasma exposure. Atomic vacancies have grown into nanopores after an additional 2 s of plasma exposure.

single carbon atom, matching the atomic model of a single-carbon atom vacancy presented in the inset. The density of vacancies was determined to be around four vacancies per 100 nm^2.

No vacancy was found in the graphene samples with hydrogen plasma treatment less than 2 min. The reason why vacancies form only after 2 min of plasma treatment is speculative. One possible explanation involves the presence of parasitic oxygen atoms in the system, which are transformed into reactive oxygen species by the plasma. Due to their preferential etching of the sp^3 hybridized PMMA, the density of these oxygen atoms might not have been sufficient to attack the graphene until most of the PMMA is eliminated (the "loading effect" in plasma etching). Simultaneously, or alternatively, the graphene surface might have become progressively hydrogenated due to the presence of the low flux of energetic ions in the plasma. The latter explanation is supported by the Raman spectroscopy results (see below). Indeed, molecular dynamic simulations[45] and experiments[46] have both shown that 5–10 eV H^+ ion bombardment leads to progressive chemisorption of hydrogen on graphene. This chemisorption process is slow, reaching saturation with a 30 % hydrogen coverage after an H^+ fluence $> 10^{16}$ ions/cm^2 [45]. The chemisorped hydrogen atoms distort the graphene surface through sp^3 hybridization, thus weakening the carbon network. Any high energy (>10 eV) ion or parasitic oxygen-based radical can then etch the hydrogenated graphene, leading to the formation of vacancies.

Dangling bonds associated with the vacancies are easily attacked by hydrogen atoms, leading to the quick etching of neighboring carbon atoms at the initial vacancies. The etching results in pores of nanometer size, which grow rapidly. As shown in Fig. 1d, once the initial vacancies are formed, formation of nanopores takes only 2 s. These pores are uniformly distributed in the sample with a density of around 6 per 100 nm^2 and their size varies between 1 nm and 3 nm (for 2 s additional plasma treatment after vacancy formation).

The time required to produce vacancies was consistent with graphene from the same batch, which have similar PMMA coverage. Difference of tens of seconds was found among different batches. Even though the duration of plasma exposure for introducing atomic vacancies in graphene varied slightly from one batch to another, once formed, the vacancies consistently grew quickly into nanometer-sized pores within 2–5 s of further plasma exposure.

Although the PMMA residues seemed to be efficiently removed by the plasma, residues of some heavier element persisted on the graphene surface. These residues are clearly visible in Fig. 1c in the form of randomly dispersed island of nanometer size even though they are not visible in the field of view in Fig. 1b. Energy dispersion spectroscopy and X-ray photoelectron spectroscopy showed these persistent residues to be SiOx (Suppl. Figs. S2 and S3), which have also been reported in previous studies [34,47].

Raman spectroscopy was performed on the graphene grids examined by HRTEM to evaluate the crystallinity and the bonding nature of the graphene modified by the plasma treatment. Fig. 2 shows Raman spectra recorded from graphene suspended in the holes of the holey carbon TEM grids. All Raman spectra exhibit the characteristic peaks of graphene, namely G and 2D. Graphene before plasma treatment (Fig. 2a) shows a sharp G and a 2D peak with a small D peak that corresponds to little presence of defects. The results confirm the good crystallinity of the sample before the plasma treatment, in agreement with the HRTEM results (Fig. 1a). The graphene under plasma treatment was monitored at 30 s intervals by Raman spectroscopy, which showed little change before 2 min (Suppl. Fig. S4). After exposing to the plasma for 2 min, the Raman spectrum shows the growth of sharp D and D′ peaks, a slight broadening and decrease in the 2D peak compared to the G peak, as well as the emergence of a D + D' combinational mode can be observed (Fig. 2b). The evolution of the Raman results indicates a change in the chemical nature of the graphene even though HRTEM analysis of this sample indicated no structural changes induced by the plasma exposure (Fig. 1b). Indeed, the Raman spectrum closely resembles published spectra of hydrogenated graphene that has been confirmed by X-ray photoelectron spectroscopy [48], [47]. In these spectra, the sharp D peak results from the disruption of the translational symmetry of the C–C sp^2 bonds and the formation of sp^3-hybridized C–H bonds in hydrogenated graphene, as expected with low energy hydrogen plasma treatments [34], [47]. The similar Raman results in Fig. 2b thus suggest that the graphene surface is hydrogenated. On the other hand, hydrogenation is difficult to detect by HRTEM, which shows only a regular graphene lattice for this sample (Fig. 1b).

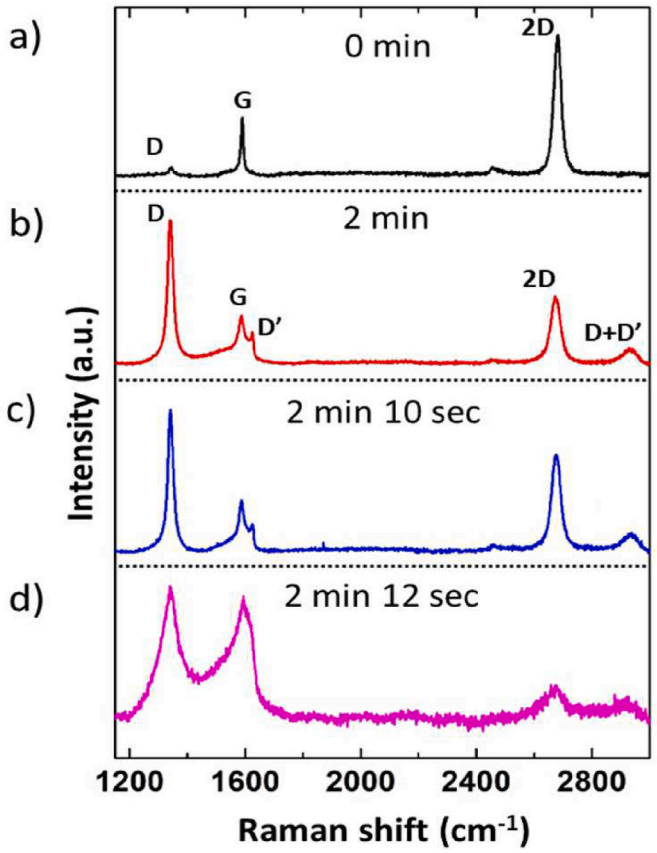

Fig. 2. Raman spectra of graphene suspended in holes in holey carbon TEM grids in Fig. 1(a–d). (a) Graphene before plasma treatment shows characteristic G and 2D peaks. (b) Graphene after 2 min of plasma treatment shows a significant increase in the D and D′ peaks, in agreement with graphene hydrogenation. (c) Graphene with atomic vacancies exhibits a profile identical to the partially hydrogenated samples. (d) Graphene with nanopores displays characteristics of defective graphene.

The Raman spectrum of the sample containing atomic vacancies (Fig. 1c and 2c) exhibits characteristics similar to those of the partially hydrogenated sample, which showed no point defects in HRTEM (Fig. 1b and 2b). This observation is particularly interesting because the Raman signal originating from monoatomic carbon vacancies in graphene closely resembles or is dominated by the signal produced by hydrogenation. Consequently, distinguishing between atomic vacancies and hydrogenation in graphene using Raman spectroscopy is challenging. In contrast, this information was evident from HRTEM (Fig. 1b and c).

The Raman spectrum of the sample with integrated nanopores (Fig. 1d and 2d) confirms the presence of highly disordered graphene features with a significant reduction in the height of the 2D peak and the broadening of the G band intensity. These Raman spectroscopy results support and complement the findings from HRTEM analysis of the samples.

We next investigated the relationship between the different structures exhibited in the graphene layers and their wetting properties during cryo-TEM sample preparation. We employed graphene TEM grids that exhibited the four typical structures (native, partially

hydrogenated, vacancy, nanopore) as support films for sample vitrification. We used the bacteriophage T5 as a test sample. These viral particles have a capsid of ~90 nm connected to a tail with fine structures (a negative stained image of T5 can be found in Suppl. Fig. S5). The large capsid makes it easy to identify the sample particles. On the other hand, the fine details of the tailpiece allows an estimation of the thickness of the ice layer; as the signal-to-noise-ratio of the image depends on the ice layer thickness, which contributes to background scattering, the resolution of the fine tail fibers would indicate thin ice.

Vitrified T5 samples were prepared on the different graphene grids to be examined by cryo-TEM. Around 4 μl of sample solution was applied onto the graphene grid in the humidity and temperature controlled Vitrobot chamber. The grid was then blotted with filter papers and plunge frozen in liquid ethane. The vitrified sample was then observed by cryo-TEM at near liquid nitrogen temperature.

Fig. 3a shows the T5 sample applied onto a graphene grid without any hydrogen plasma treatment. Ice pellets from vitrified droplets of sample solution can be observed on the graphene surface. The inherently hydrophobic graphene has impeded the sample solution from staying uniformly across its surface. Instead, the applied sample drop had broken up during blotting into droplets possibly trapped by isolated patches of impurities (e.g. PMMA), defect sites, folds or dip in the graphene layer, giving rise to the pellets observed. We note that some pellets are large enough to contain viral particles.

Fig. 3b shows the sample applied to the partially hydrogenated graphene. Numerous pellets of around 100 nm are observed on this surface, suggesting that graphene hydrogenation has increased the density of isolated hydrophilic patches. Nevertheless, the partially hydrogenated surface does not allow the formation of a continuous ice layer.

In contrast, a uniform ice layer is found on the graphene sample containing atomic defects (for both vacancies and nanopores) as shown for the vacancy created sample in Fig. 3c. On this grid, the T5 viral particles are well dispersed. This observation implies that atomic vacancies can transform the hydrophobic graphene surface into a hydrophilic one. Such a substantial change in wetting property can be attributed to an increase in graphene surface energy due to the introduction of dangling bonds through vacancy formation. When the surface energy exceeds the binding energy of water molecules, it enables the separation of water molecules, allowing water to bond with the graphene surface and spread uniformly across the surface. A similar result of uniform ice layer formation was observed on the nanopore-integrated graphene sample. These results indicate that a few dangling bonds are sufficient to increase graphene surface energy and transform a hydrophobic surface into a hydrophilic one.

Since TEM is a local technique in the microscopic scale, we further quantified the wetting properties of different graphene samples on a macroscopic scale by water contact angle measurements. An optical image was captured immediately after the application of a drop of 0.7 μL deionized water onto the graphene grids treated with various plasma treatment duration. These images displayed in Fig. 4 show the interaction between the water droplet and the graphene grids. The contact angle in Fig. 4a for graphene without hydrogen plasma treatment measures 84° characteristic of a hydrophobic surface. The partially hydrogenated sample shown in Fig. 4b maintains a hydrophobic nature, with a nearly identical contact angle of 80°. Fig. 4c shows the measurement on nanopore integrated graphene after 2 min 12 s of plasma treatment, indicating that defects (e.g. nanopores), effectively enhance

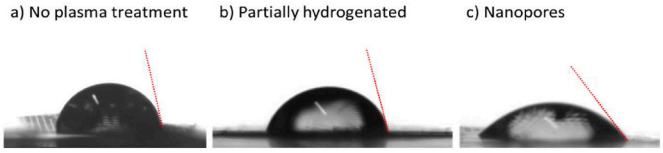

Fig. 4. Water contact angle measurement on graphene grids before and after hydrogen plasma treatment. (a) Graphene without plasma treatment is hydrophobic with a contact angle of 84°. (b) Partially hydrogenated graphene surface (2 min plasma treatment) remains hydrophobic with a similar contact angle of 80°. (c) Nanopores generated after 2 min and 12 s plasma treatment on graphene renders the surface hydrophilic with a contact angle of 58°.

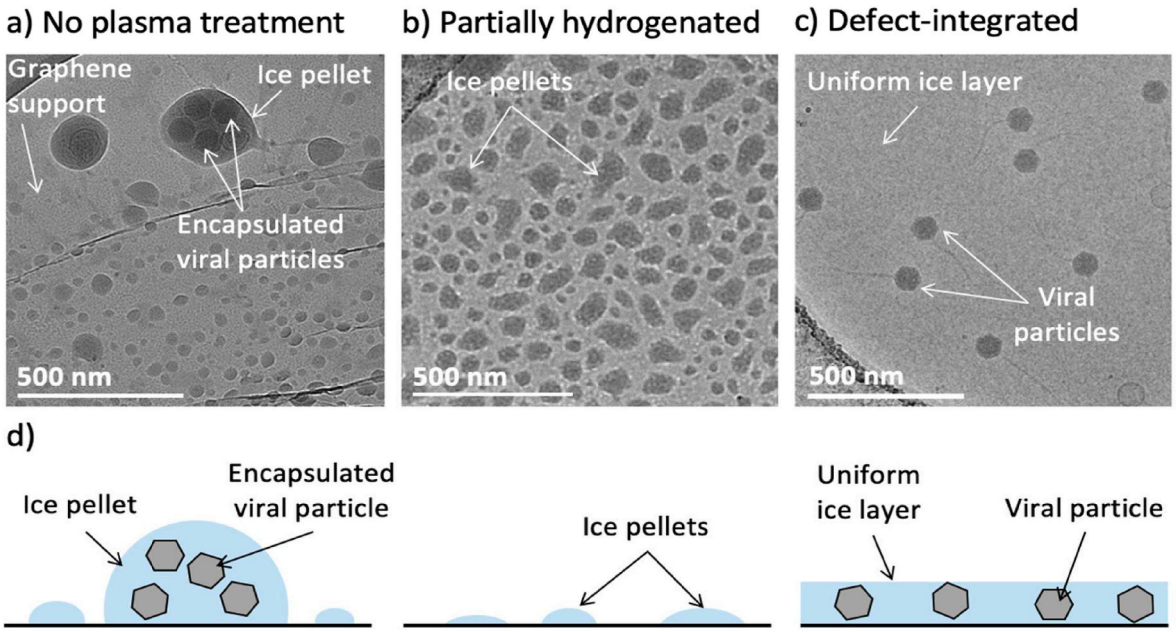

Fig. 3. Cryo-TEM images of T5 viral particles in solution applied to monolayer graphene with and without hydrogen plasma treatment. (a) Graphene without plasma treatment suspended on lacey carbon grid. Few ice pellets are formed on intrinsically hydrophobic graphene. Some viral particles are trapped in the large and round ice pellets. (b) Graphene after 2 min plasma treatment suspended on C-flat grid with 2 μm holes. Numerous small ice pellets of around 100 nm are formed on the partially hydrogenated graphene surface. No viral particles are found in these small ice pellets. (c) Graphene after plasma treatment of 2 min 10 s suspended on C-flat grid. Defect integration (atomic vacancy) transforms the hydrophobic graphene surface into a hydrophilic one, enabling uniform ice layer formation with evenly distributed viral particles. (d) Schematic drawing representing the ice formed in the three cases.

the wetting properties of graphene, resulting in a lower contact angle of 58°. The water contact angle measurements are in good agreement with the cryo-TEM results (Fig. 3).

As ice thickness is a critical parameter that impacts the processes in single particle analysis, we next investigated the behavior of nanopore-integrated graphene grids as we varied the vitreous ice thickness. In general, ice layer encompassing the sample should be thin to minimize the multiple scattering of the electrons to achieve optimal contrast for particle picking and particle alignment. On the other hand, it should be thick enough to avoid protein denaturation. The ice thickness is generally controlled by the blotting time in the vitrification process. Before plunging into liquid ethane, extra sample solution is blotted away by filter paper brought into contact with the grid. In this way, only a thin layer of sample solution remains on the grid.

Fig. 5 shows cryo-TEM images of T5 viral particles vitrified with increasing blotting time. The phage T5 is a model virus, which infects *Escherichia coli* [40]. It consists of an icosahedral capsid (90 nm in diameter) packed with DNA, connected to a 160 nm long tail tube. Fine tail fibers of around 3 nm in diameter are found in the tip complex at the distal extremity of the tail [49]. Low magnification images of the graphene suspended in the holes of the C-flat film (Fig. 5 top row) show progressively thinner ice with increasing blotting time, as expected.

Higher magnification images (Fig. 5 bottom row) confirm this trend. The T5 capsid can be readily recognized in all images. Nevertheless, whereas only the central tube of the tail can be observed easily in the first case (2 s blot time), the tail fibres can be discerned in the second case (4 s blot time), as expected for thinner ice. In the last case (6 s blot time), however, the particles appear different from those in the other images. The background is no longer homogeneous but show darker contrast around the viral particles. Some capsids also have a lighter contrast than other capsids and some do not appear symmetrical. Moreover, long, tangled fibres are found. These observations suggest that the 6 s of blotting has removed most of the buffer solution except that around the dense viral prarticles. The sample dehydration has likely damage some capsids (lighter contrast, less spherical capsids), causing them to empty their DNA (long fibres in the background) (Fig. 5c). Such thin ice would probably not be realizable as freely suspending ice using conventional holey C film alone.

Then, we tested the nanopore-integrated graphene grid for cryo-TEM data collection of the mouse serotonin 5-HT_3 receptor sample for single particle analysis. This membrane protein is a pentameric neurotransmitter-gated ion channel of ~250 kDa and is a drug target for a variety of disorders. It consists of an extracellular domain (ECD), an transmembrane domain (TMD), and an intracellular domain (ICD). The ECD is beta-sheet rich and the TMD forms an alpha-helical pore [50]. Membrane proteins often exhibit poor density and distribution in free-standing ice layer on holey TEM grid. With conventional holey carbon grids, we found that a high concentration of protein (~3 mg/ml) gave satisfactory results. Nevertheless, since the protein has a strong preference to bind the carbon film, the sample solution had to be applied twice in order to saturate the carbon film during the first application to increase the proportion of protein molecules in the holes upon the second

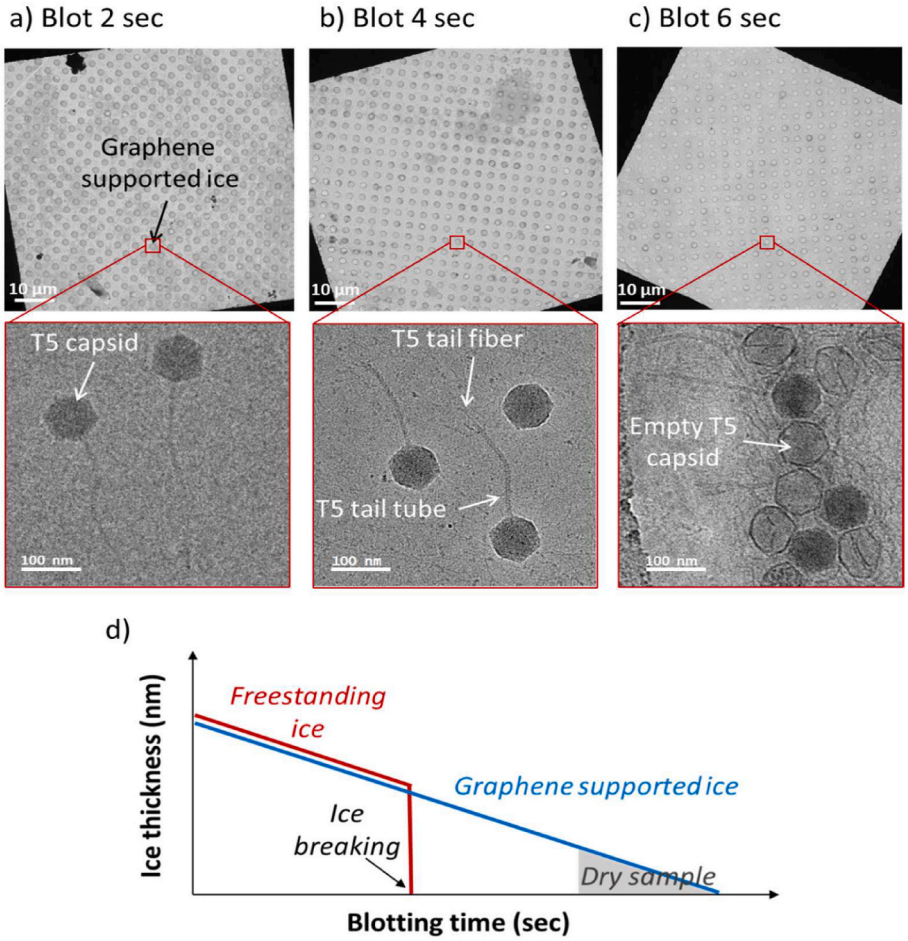

Fig. 5. Bateriophage T5 sample vitrified with increasing blotting time on hydrophilic graphene support film. (a) 2 s blotting. Capsid and tail tube of the viral particles are visible. (b) 4 s blotting. Besides the capsid and the tail tube, fine tail fibers near the tip of the tail tube are also visible. (c) 6 s blotting. Capsids appear in two different contrast. The capsids that appear lighter (less dense) are damaged and emptied of DNA. (d) Schematic of ice thickness variation with blotting time: graphene-supported ice vs freestanding ice.

sample application.

We vitrified the m5-HT_3 sample using two grids without graphene and two grids with nanopore-integrated graphene. The vitrification was carried out with the same blotting time (6 s) for the two grids without graphene and the first grid with graphene support (Fig. 7) and with reduced blotting time (4 s) for the last grid with the graphene support. Fig. 6 displays cryo- TEM images of m5-HT_3 protein particles on a grid without graphene (Fig. 6a) and on a grid with graphene support (Fig. 6b). Sample concentration used for the grids without graphene was three times higher than for the grids with graphene support (see Table 1). In Fig. 6a, protein particles are observed near the edge of the holes and on the carbon film. In contrast, protein particles are evenly distributed on the graphene support (Fig. 6b).

We compare the data processing results of the grids with or without graphene support (Fig. 7). Given that the total number of exposures/ movies acquired was different among the 4 datasets, we randomly selected 1048 exposures for each data set. From these 1048 exposures, the total number of particles with the graphene support was ~3 times higher than that without graphene support. During data processing, no significant difference was observed among the 2D class averages (Fig. 7b) obtained from data sets with and without graphene support, though a slightly better resolution of the 3D reconstruction was obtained with graphene support films based on the Fourier shell correlation estimation.

Nevertheless, it is obvious that part of the TMD with the entire ICD are missing in the reconstruction from data set 3. We speculate that the ice on the grid for data set 3 may have been too thin (this grid was blotted with filter paper for 6 s before plunge freezing vs 4 s for the grid that yielded data set 4), increasing the probability of interaction of the detergent belt around the TMD of the protein with the graphene layer or the interaction with the air-water interface. The interaction would have distorted the TMD and the small ICD, resulting in the lack of information on these domains.

4. Conclusion

The relationship between the graphene atomic structure and its wetting property has been investigated. Using a hydrogen plasma, we progressively transformed the graphene structure, which we followed using Raman spectroscopy and HRTEM. Hydrogenation of the surface was followed by the formation of vacancies, which then grew into nanopores. Cryo-TEM and contact angle measurements determined that the incorporation of defects (vacancies or nanopores) in graphene transformed the hydrophobic surface into a hydrophilic one.

The duration of plasma exposure necessary to form vacancies in the graphene was consistent for graphene from the same commercial batch but varies slightly among different batches. Thus, once the optimal duration is established for a batch, nanopores can be reliably reproduced in the graphene. The mechanical property of the nanopore-integrated graphene remains adequate as a support film as graphene remains intact in the holes of the holey carbon grid (Fig. 5). Nevertheless, prolonged plasma treatment should be avoided as the corresponding increase in size of the nanopores will lead to reduced mechanical strength manifested as broken graphene in the holes of the holey carbon film. Whereas hydrogen plasma treatment allows controlled introduction of vacancy and nanopores to the graphene surface, other more aggressive plasma treatments (e.g. air or oxygen plasma) readily generate larger pores, which weaken the graphene. In this case, bilayer or multilayer graphene should be used to ensure adequate mechanical strength as a support film [14]. These findings could advance the routine use of reliable graphene support films in cryo- TEM experiments.

With the transformed graphene as a support film, we showed that it was possible to achieve a uniform ice layer with precise control over the ice thickness in cryo-TEM TEM experiments. Vitrification of a membrane protein solubilized in detergent using the nanopore-integrated graphene support film showed a uniform distribution of particles with a higher density of particles retained on the grid than using a conventional holey carbon grid, even with a sample of lower concentration. Although the 3D reconstruction with the graphene support attained a slightly higher resolution according to the Fourier shell correlation estimate, information on part of the protein was missing in one of the data set, possibly due to the denaturation of the protein with a solution layer that became too thin with excessive blotting before vitrification. These results showed that graphene could be an asset for low-yield protein, including membrane proteins. Nonetheless, vitrification conditions need to be carefully determined for optimal protein preservation and imaging resolution, just as in the case of using conventional holey carbon films.

CRediT authorship contribution statement

Kshipra Sharma: Writing – original draft, Visualization, Validation, Project administration, Methodology, Investigation, Formal analysis, Data curation, Conceptualization. **Uriel López-Sánchez:** Writing – review & editing, Visualization, Validation, Investigation, Formal analysis, Data curation. **Hugues Nury:** Writing – review & editing, Supervision, Resources, Methodology, Investigation. **Guy Schoehn:** Writing – review & editing, Supervision, Resources, Methodology, Investigation. **Claudine Darnault:** Resources, Investigation. **Cécile**

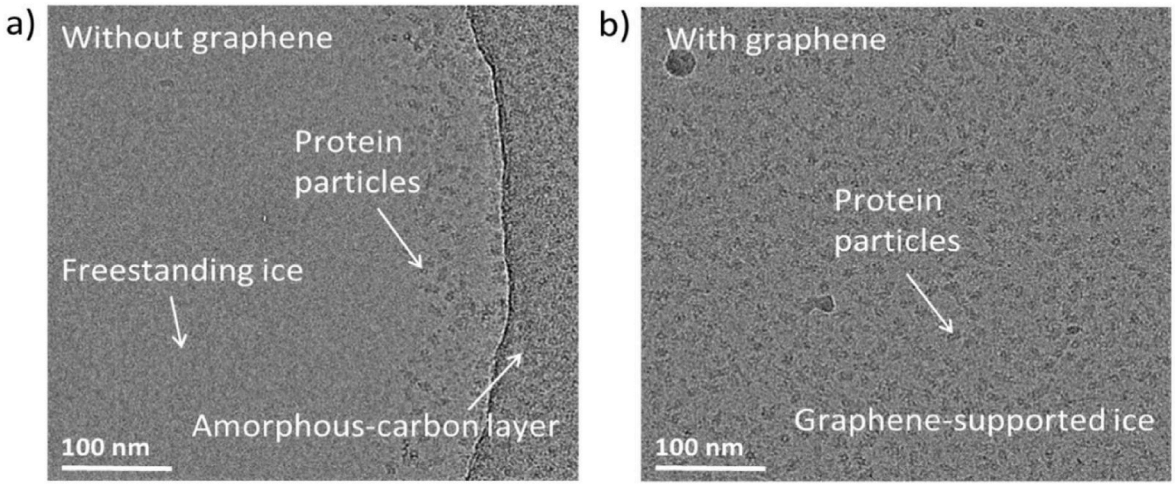

Fig. 6. Cryo-TEM images of mouse serotonin 5-HT_3 receptor. (a) Protein particles vitrified on a holey carbon C-flat grid are found at the edge of the hole and on the carbon film. (b) The protein molecules are distributed evenly across the nanopore-integrated graphene TEM grid.

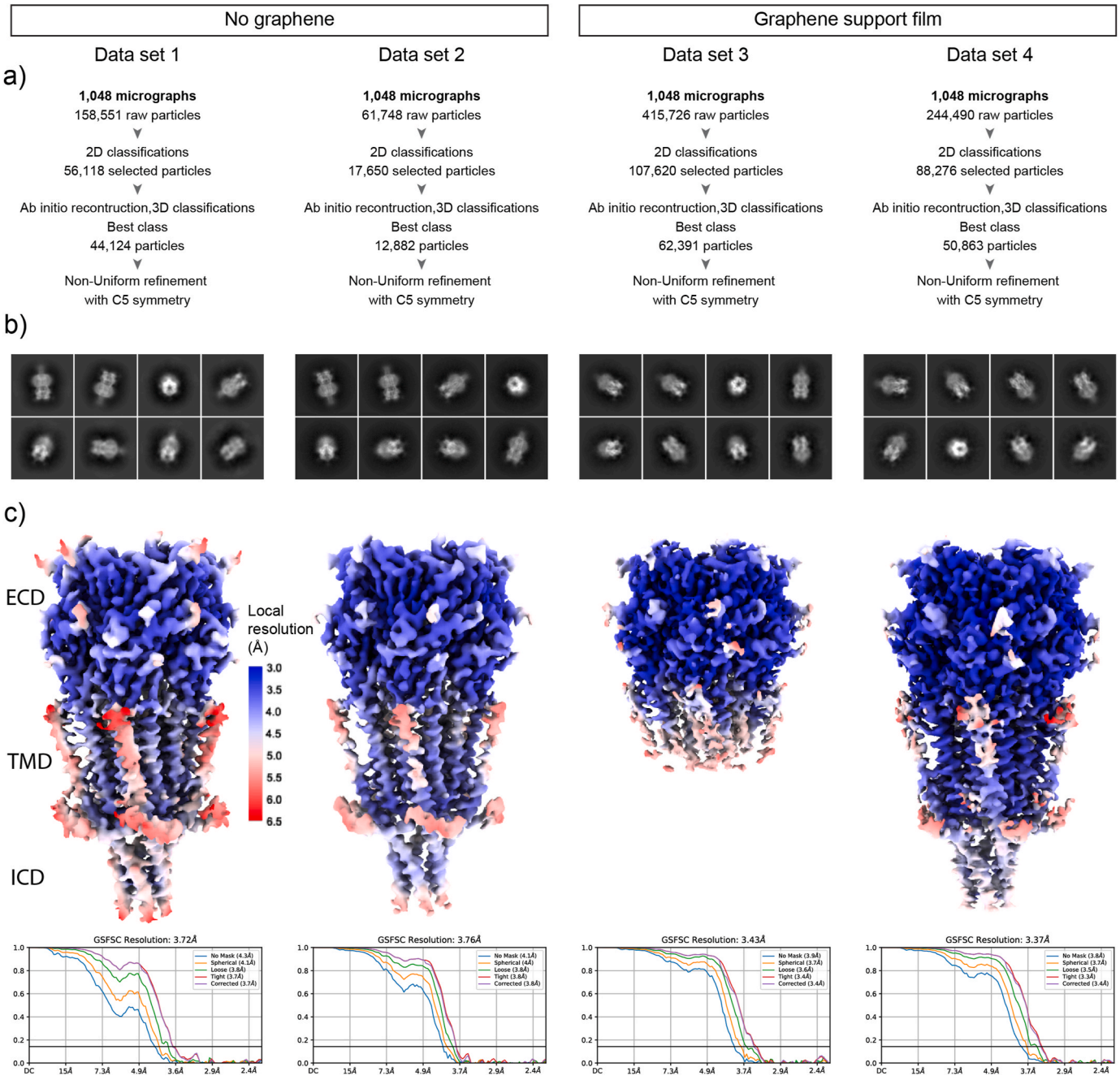

Fig. 7. Single particle analysis of the m5-HT_3 receptor from cryo-TEM datasets acquired without (Data set 1-2) and with nanopore-integrated graphene support (Data set 3-4): (a) Data processing workflow with statistics from each step of the four data sets. (b) 2D classes of the collected particles in different orientations. (c) Reconstructed 3D volumes of the protein from the four data set with color coding of the local resolution. The three domains: extracellular domain (ECD), transmembrane domain (TMD), and the intracellular domain (ICD) are resolved with recognizable secondary structures from data sets 1, 2, and 4. Information on part of the TMD and the entire ICD are lost in the reconstruction from data set 3. The resolution indicated by the gold standard Fourier shell correlation (GSFSC) is slightly better for the reconstruction obtained with the graphene support.

Table 1
Comparison of experimental parameters for cryo-TEM experiments of m5-HT_3 receptor with and without graphene support.

Sample parameters	Without graphene	With graphene
Concentration of protein sample in solution (mg/ml)	3	1
Application of specimen solution (μL)	3.5 x 2	3.5
Average number of collected particles (1048 images)	110,149	330,108

Breyton: Writing – review & editing, Supervision, Resources. **Camille Petit-Etienne:** Resources, Formal analysis. **Céline Vergnaud:** Resources, Investigation, Formal analysis. **Wai Li Ling:** Writing – review & editing, Validation, Supervision, Resources, Project administration, Methodology, Investigation, Funding acquisition, Data curation, Conceptualization. **Gilles Cunge:** Writing – review & editing, Validation, Supervision, Resources, Methodology, Investigation, Funding acquisition, Data curation, Conceptualization. **Hanako Okuno:** Writing – review & editing, Writing – original draft, Validation, Supervision, Resources, Project administration, Methodology, Investigation, Funding acquisition, Data curation, Conceptualization.

Declaration of competing interest

The authors declare that they have no known competing financial interests or personal relationships that could have appeared to influence the work reported in this paper.

Acknowledgments

We acknowledge the financial support of the Cross-Disciplinary Program on Instrumentation and Detection of CEA, the French Alternative Energies and Atomic Energy Commission. This work used the platforms of the Grenoble Instruct-ERIC center (ISBG; UAR 3518 CNRS-CEA-UGA-EMBL) within the Grenoble Partnership for Structural Biology (PSB) supported by FRISBI (ANR-10-INBS-05-02) and GRAL, a project of the University Grenoble Alpes graduate school (Ecoles Universitaires de Recherche) CBH-EUR-GS (ANR-17-EURE-0003). The IBS Electron Microscope facility is supported by the Auvergne RhôneAlpes Region, the Fonds Feder, the Fondation pour la Recherche Médicale and GIS IBiSA. This work was partly supported by the French RENATECH network and the CEA CFR.

Appendix A. Supplementary data

Supplementary data to this article can be found online at https://doi.org/10.1016/j.carbon.2024.119625.

References

[1] K.S. Novoselov, A.K. Geim, S.V. Morozov, D. Jiang, Y. Zhang, S.V. Dubonos, I. V. Grigorieva, A.A. Firsov, Electric field effect in atomically thin carbon films, Science 306 (5696) (2004) 666–669, https://doi.org/10.1126/science.1102896.
[2] A.A. Balandin, S. Ghosh, W. Bao, I. Calizo, D. Teweldebrhan, F. Miao, C.N. Lau, Superior thermal conductivity of single-layer graphene, Nano Lett. 8 (3) (2008) 902–907, https://doi.org/10.1021/nl0731872.
[3] M.D. Stoller, S. Park, Y. Zhu, J. An, R.S. Ruoff, Graphene-based ultracapacitors, Nano Lett. 8 (10) (2008) 3498–3502, https://doi.org/10.1021/nl802558y.
[4] P. Blake, P.D. Brimicombe, R.R. Nair, T.J. Booth, D. Jiang, F. Schedin, L. A. Ponomarenko, S.V. Morozov, H.F. Gleeson, E.W. Hill, A.K. Geim, K. S. Novoselov, Graphene-based liquid crystal device, Nano Lett. 8 (6) (2008) 1704–1708, https://doi.org/10.1021/nl080649i.
[5] C. Lee, X. Wei, J.W. Kysar, J. Hone, Measurement of the elastic properties and intrinsic strength of monolayer graphene, Science 321 (5887) (2008) 385–388, https://doi.org/10.1126/science.1157996.
[6] S. Sinha, J.H. Warner, Recent progress in using graphene as an ultrathin transparent support for transmission electron microscopy, Small Struct 2 (4) (2021) 2000049, https://doi.org/10.1002/sstr.202000049.
[7] R.S. Pantelic, J.C. Meyer, U. Kaiser, H. Stahlberg, The application of graphene as a sample support in transmission electron microscopy, Solid State Commun. 152 (15) (2012) 1375–1382, https://doi.org/10.1016/j.ssc.2012.04.038.
[8] T.M. Duong, K. Sharma, F. Agnese, J.-L. Rouviere, H. Okuno, S. Pouget, P. Reiss, W. L. Ling, Practice of electron microscopy on nanoparticles sensitive to radiation damage: CsPbBr3 nanocrystals as a case study, Front. Chem. 10 (2022), https://doi.org/10.3389/fchem.2022.1058620.
[9] K. Naydenova, P. Jia, C.J. Russo, Cryo-EM with sub–1 Å specimen movement, Science 370 (6513) (2020) 223–226, https://doi.org/10.1126/science.abb7927.
[10] L. Zheng, N. Liu, X. Gao, W. Zhu, K. Liu, C. Wu, R. Yan, J. Zhang, X. Gao, Y. Yao, B. Deng, J. Xu, Y. Lu, Z. Liu, M. Li, X. Wei, H.-W. Wang, H. Peng, Uniform thin ice on ultraflat graphene for high-resolution cryo-EM, Nat. Methods 20 (1) (2023) 123–130, https://doi.org/10.1038/s41592-022-01693-y.
[11] N. Liu, Z. Jincan, Y. Chen, C. Liu, X. Zhang, K. Xu, J. Wen, Z. Luo, S. Chen, P. Gao, K. Jia, Z. Liu, H. Peng, H. Wang, Bioactive functionalized monolayer graphene for high resolution cryo-EM, J. Am. Chem. Soc. 141 (2019), https://doi.org/10.1021/jacs.8b13038.
[12] Y. Han, X. Fan, H. Wang, F. Zhao, C.G. Tully, J. Kong, N. Yao, N. Yan, High-yield monolayer graphene grids for near-atomic resolution cryoelectron microscopy, Proc. Natl. Acad. Sci. USA 117 (2) (2020) 1009–1014, https://doi.org/10.1073/pnas.1919114117.
[13] K. Naydenova, M.J. Peet, C.J. Russo, Multifunctional graphene supports for electron cryomicroscopy, Proc. Natl. Acad. Sci. USA 116 (24) (2019) 11718–11724, https://doi.org/10.1073/pnas.1904766116.
[14] L. Zheng, N. Liu, Y. Liu, N. Li, J. Zhang, C. Wang, W. Zhu, Y. Chen, D. Ying, J. Xu, Z. Yang, X. Gao, J. Tang, X. Wang, Z. Liang, R. Zou, Y. Li, P. Gao, X. Wei, H.-W. Wang, H. Peng, Atomically thin bilayer janus membranes for cryo-electron microscopy, ACS Nano 15 (10) (2021) 16562–16571, https://doi.org/10.1021/acsnano.1c06233.
[15] C.J. Russo, L.A. Passmore, Controlling protein adsorption on graphene for cryo-EM using low-energy hydrogen plasmas, Nat. Methods 11 (6) (2014) 649–652, https://doi.org/10.1038/nmeth.2931.
[16] R. Kato, Y. Hatano, N. Kasahata, C. Sato, K. Suenaga, M. Hasegawa, High-precision thickness control of ice layer on CVD grown bilayer graphene for cryo-TEM, Carbon 160 (2020) 107–112, https://doi.org/10.1016/j.carbon.2020.01.010.
[17] E. D'Imprima, D. Floris, M. Joppe, R. Sánchez, M. Grininger, W. Kühlbrandt, Protein denaturation at the air-water interface and how to prevent it, Elife 8 (2019) e42747, https://doi.org/10.7554/eLife.42747.
[18] S. Wang, Y. Zhang, N. Abidi, L. Cabrales, Wettability and surface free energy of graphene films, Langmuir 25 (18) (2009) 11078–11081, https://doi.org/10.1021/la901402f.
[19] O. Leenaerts, B. Partoens, F.M. Peeters, Water on graphene: hydrophobicity and dipole moment using density functional theory, Phys. Rev. B 79 (23) (2009) 235440, https://doi.org/10.1103/PhysRevB.79.235440.
[20] A. Kozbial, Z. Li, C. Conaway, R. McGinley, S. Dhingra, V. Vahdat, F. Zhou, B. D'Urso, H. Liu, L. Li, Study on the surface energy of graphene by contact angle measurements, Langmuir 30 (28) (2014) 8598–8606, https://doi.org/10.1021/la5018328.
[21] A. Boland, T.G. Martin, Z. Zhang, J. Yang, X. Bai, L. Chang, S.H.W. Scheres, D. Barford, Cryo-EM structure of a metazoan separase–securin complex at near-atomic resolution, Nat. Struct. Mol. Biol. 24 (4) (2017) 414–418, https://doi.org/10.1038/nsmb.3386.
[22] P. Nickl, T. Hilal, D. Olal, I.S. Donskyi, J. Radnik, K. Ludwig, R. Haag, A new support film for cryo electron microscopy protein structure analysis based on covalently functionalized graphene, Small 19 (8) (2023) 2205932, https://doi.org/10.1002/smll.202205932.
[23] S. Plana-Ruiz, A. Gomez-Perez, M. Budayova-Spano, D.L. Foley, J. Portillo-Serra, E. Rauch, E. Grivas, D. Housset, P. Pratim Das, M.L. Taheri, S. Nicolopoulos, W. L. Ling, High-resolution electron diffraction of hydrated protein crystals at room temperature. https://doi.org/10.1021/acsnano.3c05378, 2023.
[24] Q. Xu, W. Zhang, Q. Xu, W. Zhang, Next-Generation Graphene-Based Membranes for Gas Separation and Water Purifications, IntechOpen, 2016, https://doi.org/10.5772/64396.
[25] D. Jiang, V.R. Cooper, S. Dai, Porous graphene as the ultimate membrane for gas separation, Nano Lett. 9 (12) (2009) 4019–4024, https://doi.org/10.1021/nl9021946.
[26] S.P. Koenig, L. Wang, J. Pellegrino, J.S. Bunch, Selective molecular sieving through porous graphene, Nat. Nanotechnol. 7 (11) (2012) 728–732, https://doi.org/10.1038/nnano.2012.162.
[27] Geankoplis, C. J. Transport Processes and Separation Process Principles:(Includes Unit Operations)/Christie John Geankoplis.
[28] R.W. Baker, Research needs in the membrane separation industry: looking back, looking forward, J. Membr. Sci. 362 (1) (2010) 134–136, https://doi.org/10.1016/j.memsci.2010.06.028.
[29] R.W. Baker, K. Lokhandwala, Natural gas processing with membranes: an overview, Ind. Eng. Chem. Res. 47 (7) (2008) 2109–2121, https://doi.org/10.1021/ie071083w.
[30] D. Hug, S. Zihlmann, M.K. Rehmann, Y.B. Kalyoncu, T.N. Camenzind, L. Marot, K. Watanabe, T. Taniguchi, D.M. Zumbühl, Anisotropic etching of graphite and graphene in a remote hydrogen plasma, Npj 2D Mater. Appl. 1 (1) (2017) 1–6, https://doi.org/10.1038/s41699-017-0021-7.
[31] B. McCarroll, D.W. McKee, The reactivity of graphite surfaces with atoms and molecules of hydrogen, oxygen and nitrogen, Carbon 9 (3) (1971) 301–311, https://doi.org/10.1016/0008-6223(71)90049-2.
[32] L. Xie, L. Jiao, H. Dai, Selective etching of graphene edges by hydrogen plasma, J. Am. Chem. Soc. 132 (42) (2010) 14751–14753, https://doi.org/10.1021/ja107071g.
[33] A. Felten, A. Eckmann, J.-J. Pireaux, R. Krupke, C. Casiraghi, Controlled modification of mono- and bilayer graphene in O2, H2 and CF4 plasmas, Nanotechnology 24 (35) (2013) 355705, https://doi.org/10.1088/0957-4484/24/35/355705.
[34] G. Cunge, D. Ferrah, C. Petit-Etienne, A. Davydova, H. Okuno, D. Kalita, V. Bouchiat, O. Renault, Dry efficient cleaning of poly-methyl-methacrylate residues from graphene with high-density H2 and H2-N2 plasmas, J. Appl. Phys. 118 (12) (2015) 123302, https://doi.org/10.1063/1.4931370.
[35] E. Aréou, G. Cartry, J.-M. Layet, T. Angot, Hydrogen-graphite interaction: experimental evidences of an adsorption barrier, J. Chem. Phys. 134 (1) (2011) 014701, https://doi.org/10.1063/1.3518981.
[36] G.H. Ryu, J. Lee, D. Kang, H.J. Jo, H.S. Shin, Z. Lee, Effects of dry oxidation treatments on monolayer graphene, 2D Mater. 4 (2) (2017) 024011, https://doi.org/10.1088/2053-1583/aa75a9.
[37] H. Park, C. Lim, C.-J. Lee, J. Kang, J. Kim, M. Choi, H. Park, Optimized poly(methyl methacrylate)-mediated graphene-transfer process for fabrication of high-quality graphene layer, Nanotechnology 29 (41) (2018) 415303, https://doi.org/10.1088/1361-6528/aad4d9.
[38] Z. Cheng, Q. Zhou, C. Wang, Q. Li, C. Wang, Y. Fang, Toward intrinsic graphene surfaces: a systematic study on thermal annealing and wet-chemical treatment of SiO_2 -supported graphene devices, Nano Lett. 11 (2) (2011) 767–771, https://doi.org/10.1021/nl103977d.
[39] C. Gong, H.C. Floresca, D. Hinojos, S. McDonnell, X. Qin, Y. Hao, S. Jandhyala, G. Mordi, J. Kim, L. Colombo, R.S. Ruoff, M.J. Kim, K. Cho, R.M. Wallace, Y. J. Chabal, Rapid selective etching of PMMA residues from transferred graphene by carbon dioxide, J. Phys. Chem. C 117 (44) (2013) 23000–23008, https://doi.org/10.1021/jp408429v.

[40] Y. Zivanovic, F. Confalonieri, L. Ponchon, R. Lurz, M. Chami, A. Flayhan, M. Renouard, A. Huet, P. Decottignies, A.R. Davidson, C. Breyton, P. Boulanger, Insights into bacteriophage T5 structure from analysis of its morphogenesis genes and protein components, J. Virol. 88 (2) (2014) 1162–1174, https://doi.org/10.1128/jvi.02262-13.

[41] K. Grychowska, U. López-Sánchez, M. Vitalis, G. Canet, G. Satała, A. Olejarz-Maciej, J. Gołębiowska, R. Kurczab, W. Pietruś, M. Kubacka, C. Moreau, M. Walczak, K. Blicharz-Futera, O. Bento, X. Bantreil, G. Subra, A.J. Bojarski, F. Lamaty, C. Becamel, C. Zussy, S. Chaumont-Dubel, P. Popik, H. Nury, P. Marin, L. Givalois, P. Zajdel, Superiority of the triple-acting 5-ht6r/5-ht3r antagonist and MAO-B reversible inhibitor PZ-1922 over 5-ht6r antagonist intepirdine in alleviation of cognitive deficits in rats, J. Med. Chem. 66 (21) (2023) 14928–14947, https://doi.org/10.1021/acs.jmedchem.3c01482.

[42] T. Wagner, F. Merino, M. Stabrin, T. Moriya, C. Antoni, A. Apelbaum, P. Hagel, O. Sitsel, T. Raisch, D. Prumbaum, D. Quentin, D. Roderer, S. Tacke, B. Siebolds, E. Schubert, T.R. Shaikh, P. Lill, C. Gatsogiannis, S. Raunser, SPHIRE-crYOLO is a fast and accurate fully automated particle picker for cryo-EM, Commun. Biol. 2 (1) (2019) 1–13, https://doi.org/10.1038/s42003-019-0437-z.

[43] A. Punjani, J.L. Rubinstein, D.J. Fleet, M.A. Brubaker, Algorithms for rapid unsupervised cryo-EM structure determination, Nat. Methods 14 (3) (2017) 290–296, https://doi.org/10.1038/nmeth.4169.

[44] E.F. Pettersen, T.D. Goddard, C.C. Huang, G.S. Couch, D.M. Greenblatt, E.C. Meng, T.E. Ferrin, UCSF chimera–a visualization system for exploratory research and analysis, J. Comput. Chem. 25 (13) (2004) 1605–1612, https://doi.org/10.1002/jcc.20084.

[45] A. Davydova, E. Despiau-Pujo, G. Cunge, D.B. Graves, Etching mechanisms of graphene nanoribbons in downstream H_2 plasmas: insights from molecular dynamics simulations, J. Phys. Appl. Phys. 48 (19) (2015) 195202, https://doi.org/10.1088/0022-3727/48/19/195202.

[46] R. Balog, B. Jørgensen, L. Nilsson, M. Andersen, E. Rienks, M. Bianchi, M. Fanetti, E. Lægsgaard, A. Baraldi, S. Lizzit, Z. Sljivancanin, F. Besenbacher, B. Hammer, T. G. Pedersen, P. Hofmann, L. Hornekær, Bandgap opening in graphene induced by patterned hydrogen adsorption, Nat. Mater. 9 (4) (2010) 315–319, https://doi.org/10.1038/nmat2710.

[47] D. Ferrah, O. Renault, D. Marinov, J. Arias-Zapata, N. Chevalier, D. Mariolle, D. Rouchon, H. Okuno, V. Bouchiat, G. Cunge, CF_4/H_2 plasma cleaning of graphene regenerates electronic properties of the pristine material, ACS Appl. Nano Mater. 2 (3) (2019) 1356–1366, https://doi.org/10.1021/acsanm.8b02249.

[48] J. Guillemette, S.S. Sabri, B. Wu, K. Bennaceur, P.E. Gaskell, M. Savard, P. L. Lévesque, F. Mahvash, A. Guermoune, M. Siaj, R. Martel, T. Szkopek, G. Gervais, Quantum Hall effect in hydrogenated graphene, Phys. Rev. Lett. 110 (17) (2013) 176801, https://doi.org/10.1103/PhysRevLett.110.176801.

[49] R. Linares, C.-A. Arnaud, G. Effantin, C. Darnault, N.H. Epalle, E. Boeri Erba, G. Schoehn, C. Breyton, Structural basis of bacteriophage T5 infection trigger and *E. Coli* cell wall perforation, Sci. Adv. 9 (12) (2023) eade9674, https://doi.org/10.1126/sciadv.ade9674.

[50] G. Hassaine, C. Deluz, L. Grasso, R. Wyss, M.B. Tol, R. Hovius, A. Graff, H. Stahlberg, T. Tomizaki, A. Desmyter, C. Moreau, X.-D. Li, F. Poitevin, H. Vogel, H. Nury, X-ray structure of the mouse serotonin 5-HT3 receptor, Nature 512 (7514) (2014) 276–281, https://doi.org/10.1038/nature13552.